Liquid-Phase Synthesis of Highly Deformable and Air-Stable Sn-Substituted Li₃PS₄ for All-Solid-State Batteries Fabricated and Operated under Low Pressures

Jehoon Woo, Yong Bae Song, Hiram Kwak, Seunggoo Jun, Bo Yeong Jang, Juhyoun Park, Kyu Tae Kim, Changhyun Park, Chanhee Lee, Kern-Ho Park, Hyun-Wook Lee, and Yoon Seok Jung*

The liquid-phase synthesis (LS) of sulfide solid electrolytes (SEs) has promising potential for mass production of practical all-solid-state Li batteries (ASLBs). However, their accessible SE compositions are mostly metal-free. Moreover, liquid-phase-synthesized-SEs (LS-SEs) suffer from high electronic conductivity due to carbon impurities, resulting in below-par electrochemical performance of ASLBs. Here, the LS of highly deformable and air-stable Li$_{3+x}$P$_{1-x}$Sn$_x$S$_4$ (0.19 mS cm^{-1}) using 1,2-ethylene diamine-1,2-ethanedithiol with tetrahydrofuran is reported. A low heat-treatment temperature (260 °C) prevents the carbonization of organic residues. Importantly, a remarkable enhancement in the deformability of LS-SEs compared to that of conventional solid-state-synthesized SEs (SS-SEs) is identified for the first time. LiNi$_{0.7}$Co$_{0.15}$Mn$_{0.15}$O$_2$ electrodes employing LS-SEs in ASLBs significantly outperform those using SS-SEs, notably when assembled under a low fabricating pressure (148 vs 370 MPa, e.g., capacity loss: 2 vs 41 mA h g^{-1}) or tested under a low operating pressure (12 or 3 MPa), which is attributed to reduced electrochemo-mechanical effects. Finally, when employing SEs that are exposed to air (dew point of −20 °C), LiNi$_{0.7}$Co$_{0.15}$Mn$_{0.15}$O$_2$ electrodes employing SEs with Sn-substituted composition or prepared by LS exhibit significantly better capacity retention than conventional SEs with Sn-free composition or prepared by SS (e.g., 92.2% for LS-Li$_{3.2}$P$_{0.8}$Sn$_{0.2}$S$_4$ vs 32.5% for SS-Li$_3$PS$_4$).

1. Introduction

Solidifying electrolytes with inorganic superionic conductors is considered a promising means to stabilize high-capacity electrodes (e.g., Li metal anodes) and improve the safety of Li batteries.[1–11] In particular, highly conductive sulfide solid electrolytes (SEs) are mechanically deformable, which allows for scalable fabrication of practical all-solid-state Li batteries (ASLBs) by simple cold-pressing processes, such as isostatic pressing, areal pressing, and roll-pressing.[3,7,12,13] A critical drawback of sulfide SEs is their poor chemical stability toward atmospheric air; upon exposure to atmospheric air, they are degraded with the release of toxic H$_2$S.[3,14] The substitution of phosphorus with metals, such as Sn and Sb, has been effective in alleviating the reactivity of sulfide SEs with air (Table S1, Supporting Information), which can be explained via hard and soft acid and base theory.[15–20]

Similar to other types of ceramic electrolytes, solid-state syntheses (SS), such as mechanochemical methods, high-temperature solid-state reactions, and melt-quenching methods, are also commonly used for the preparation of sulfide SEs.[3,7] On the other hand, Liang et al. first reported that β-Li$_3$PS$_4$ could be synthesized from a suspended solution of Li$_2$S and P$_2$S$_5$ in tetrahydrofuran (THF).[21] Since then, liquid-phase (or wet-chemical) syntheses (LS) and/or processing of sulfide SEs have been extensively investigated.[21–35] Organic solvents used in LS partially or fully dissolve the SE precursors and aid their dispersion during mechanical stirring. This feature has the potential of saving time and energy for the reaction and thus makes LS suitable for the mass production of sulfide SEs.[3,22–24] Moreover, the morphology and particle size of sulfide SEs can be controlled using LS.[21,27,36]

For the LS of sulfide SEs, solvents that have adequate dissolving power for precursors while being free from irreversible reactions are necessary.[14,22–24,37–39] Based on these criteria, appropriate solvents can be selected, and the LS of sulfide SEs using various solvents, such as THF,[21,28,29] acetonitrile,[29,30]

J. Woo, Y. B. Song, H. Kwak, S. Jun, B. Y. Jang, J. Park, K. T. Kim, Y. S. Jung
Department of Chemical and Biomolecular Engineering
Yonsei University
Seoul 03722, South Korea
E-mail: yoonsjung@yonsei.ac.kr
C. Park, C. Lee, H.-W. Lee
School of Energy and Chemical Engineering Ulsan National Institute of Science and Technology (UNIST)
Ulsan 44919, South Korea
K.-H. Park
Advanced Battery Research Center
Korea Electronics Technology Institute
Seongnam 13509, South Korea

**ADVANCED
SCIENCE NEWS**

www.advancedsciencenews.com

**ADVANCED
ENERGY
MATERIALS**

www.advenergymat.de

ethyl propionate,[31] ethyl acetate,[32] and 1,2-dimethox-yethane,[33] has been reported. However, thus far, sulfide SE materials for LS have been restricted mostly to metal-free compositions, such as binary Li_2S-P_2S_5 and ternary Li_2S-P_2S_5-LiX (X = Cl, Br, I).[3,21,22,31,32,40] This restriction is because of the poor solubility of metal sulfide precursors in conventional solvents. Recently, our group reported a universal solution synthesis of sulfide SEs using an Alkahest solvent, a binary mixture of 1,2-ethylenediamine (EDA) and 1,2-ethanedithiol (EDT) (or EDA–ethanethiol mixture). Owing to the strong dissolving power of EDA–EDT, various sulfide SEs (Li_6PS_5Cl, $Li_{10}GeP_2S_{12}$, and $Na_{11}Sn_2PS_{12}$) can be prepared via LS.[41] However, the residual carbon impurities in SEs, originating from the solvents, remain a critical problem for not only Alkahest-based solution synthesis but also conventional LS. They increase the electronic conductivity of SEs, accelerate side reactions, and impede interfacial ionic conduction in ASLB cells.

Although sulfide SEs are mechanically sinterable, the extremely high pressure required for compaction (e.g., above 300 MPa) remains a technical challenge for the mass production of ASLBs.[13,42,43] Moreover, most lab-scale ASLB cells have been tested under unrealistically high operating (or stack) pressures (e.g., ≈70 MPa), which blurs serious electrochemo-mechanical degradation.[43–45] In this regard, the material design of SEs for controlling their mechanical properties is imperative for practical ASLBs.[43,46,47]

Herein, we report a highly deformable and air-stable $Li_{3.2}P_{0.8}Sn_{0.2}S_4$ (LPSnS) prepared by LS using EDA–EDT with THF. Using the strong dissolving power of EDA–EDT, access to a metal-containing composition (LPSnS) that showed superior air stability compared with the conventional metal-free composition (Li_3PS_4 (LPS)) was enabled. Moreover, the chronic carbon impurity problem associated with LS-SEs can be avoided by selecting a composition that requires a low heat-treatment (HT) temperature of 260 °C. Importantly, it was demonstrated that the deformability of LS-SEs is significantly superior to that of solid-state-synthesized SEs (SS-SEs), by complementary analysis using scanning electron microscopy (SEM) and nano-indentation measurements. Elemental analysis and cryogenic-transmission electron microscopy (cryo-TEM) suggest that marginal amounts of organic species are responsible for the excellent deformability of the LS-SEs. When tested in $LiNi_{0.7}Co_{0.15}Mn_{0.15}O_2$ (NCM)/Li–In ASLB cells at 30 °C, the LS-SEs exhibited remarkably better electrochemical performance when assembled under lower fabricating pressures (148 vs 370 MPa) or tested under lower operating pressures (12 or 3 vs 70 MPa).

2. Results and Discussion

The LS of LPSnS proceeded in a suspended solution, wherein the precursors Li_2S, P_2S_5, and SnS_2 were dissolved in a mixture of EDA–EDT and THF, as illustrated in **Figure 1**a. In EDA–EDT, proton transfer from the acidic EDT to the basic EDA is favored, generating a thiolate anion with strong nucleophilicity.[41] Consequently, SnS_2 can dissolve and participate in the liquid-phase reaction. Moreover, using THF as a stirring mediator, a minimal
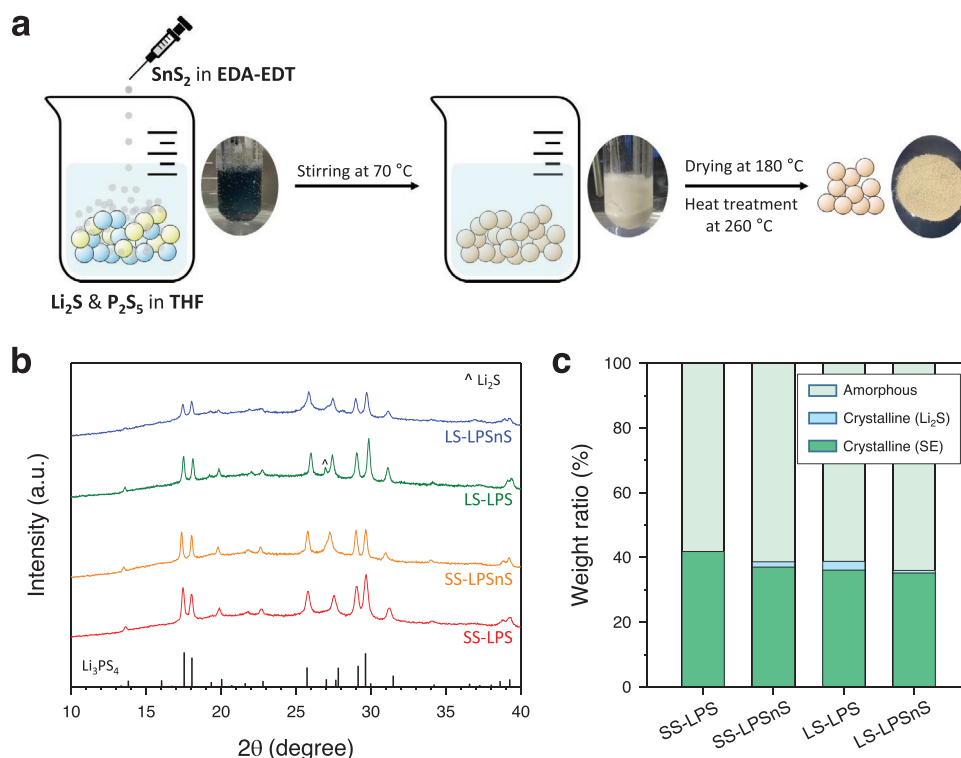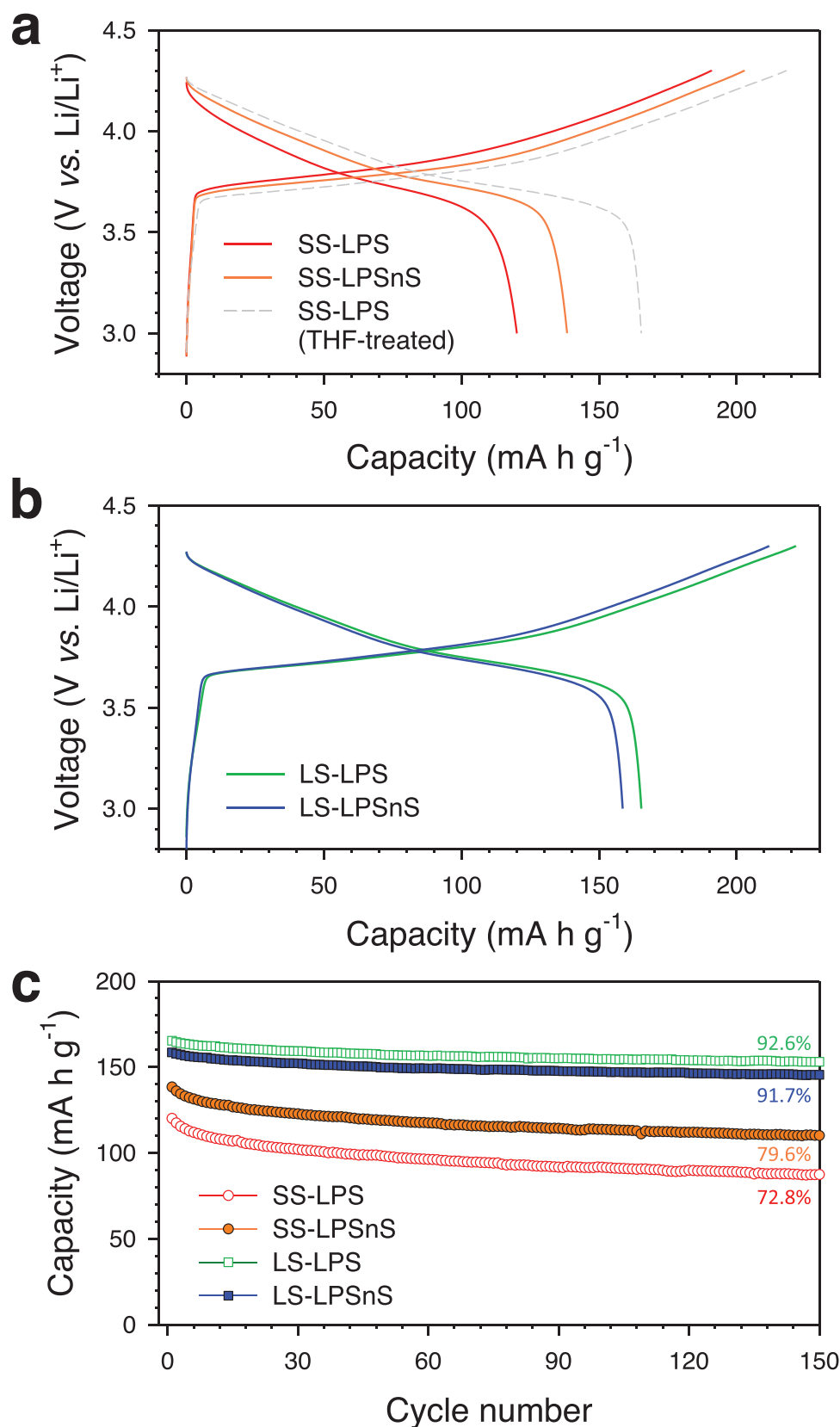

Figure 1. Liquid-phase synthesis of $Li_{3.2}P_{0.8}Sn_{0.2}S_4$ using THF and EDA–EDT. a) Schematic for the preparation of $Li_{3.2}P_{0.8}Sn_{0.2}S_4$ by liquid-phase synthesis using THF and EDA–EDT. b) XRD patterns of Li_3PS_4 and $Li_{3.2}P_{0.8}Sn_{0.2}S_4$ prepared by conventional solid-state synthesis or liquid-phase synthesis. c) Composition of amorphous and crystalline phases determined by XRD analysis.

amount of EDA–EDT was used. The optimized volume required for EDA–EDT was 3.67 µL for every gram of SE precursors. Using an extremely low amount of EDA–EDT (e.g., 2.75 µL g^{-1}) resulted in the aggregation of unreacted Li_2S (Figure S1, Supporting Information). When the liquid-phase reaction proceeded using only THF, SnS_2 remained unreacted in the presence of unknown impurity phases, as confirmed by the distinct signals in the XRD pattern (Figure S2, Supporting Information). When only EDA–EDT (11 µL g^{-1}) was used for the liquid-phase reaction, the targeted β-Li_3PS_4 phase was obtained (Figure S2, Supporting Information).[48] However, NCM electrodes employing the as-prepared LPSnS as the catholyte exhibited a poor electrochemical performance; a low first discharge capacity of 112 mA h g^{-1} at 0.2C and 30 °C was observed (Figure S3, Supporting Information). This result is significantly poorer than that of LS-LPSnS obtained using an EDA–EDT/THF solvent mixture (159 mA h g^{-1}), which is discussed below. The LPSnS powder prepared using only EDA–EDT was significantly darker than that prepared using EDA–EDT/THF (Figure S4, Supporting Information), indicating the presence of significant amounts of organic impurities.[41] An SEM image of the LPSnS powder prepared using EDA–EDT/THF exhibits spherical primary particles of 200–300 nm (Figure S5, Supporting Information).

In this study, four samples, SS-LPS, SS-LPSnS, LS-LPS, and LS-LPSnS, prepared using two different synthetic protocols (SS vs LS) or with two different compositions (Li_3PS_4 (LPS) vs LPSnS ($Li_{3.2}P_{0.8}Sn_{0.2}S_4$) were extensively compared (Table S2, Supporting Information). SS proceeded by the ball-milling of the precursors, followed by HT at 240 °C. The Li^+ conductivity was measured using Ti/SE/Ti symmetric cells by the AC method, and the corresponding Arrhenius plots are shown in Figure S6, Supporting Information. SS-LPS and SS-LPSnS exhibit Li^+ conductivities of 0.41 and 0.77 mS cm^{-1} at 30 °C, respectively, which agrees with those previously reported.[18] LS-LPS and LS-LPSnS showed Li^+ conductivities of 0.24 and 0.19 mS cm^{-1}, respectively. The Li^+ conductivity of the LS samples is lower than that of the SS samples because of the presence of impurities.[23] The electronic conductivities of the LS-SEs were sufficiently low (LS-LPS: 4.7×10^{-10} S cm^{-1}, LS-LPSnS: 1.2×10^{-10} S cm^{-1}, Table S2, Supporting Information) because the HT temperature of 260 °C was not high enough for carbonization.[41] Figure 1b shows the XRD patterns of the SE samples. The characteristic peak positions for all samples were identical and matched those of β-Li_3PS_4.[48] However, the broad XRD patterns reflect poor crystallinity, which is typical of glass-ceramic materials.[49,50] Thus, quantitative analyses of crystalline and amorphous phases were performed utilizing a mixture of SE and ZnO as a reference material (1:1 weight ratio) using the whole powder pattern fitting technique.[51] X-ray Rietveld refinement profiles obtained for the analyses are shown in Figure S7, Supporting Information, and the quantitative analysis results are displayed in Figure 1c and Table S3, Supporting Information. All SE samples contained similar amounts of crystalline SE phases (≈40 wt%), thus confirming their similar crystallinity. This value is significantly lower than that of argyrodite Li_6PS_5Cl prepared at higher temperatures of >500 °C (≈60 wt%).[51] The crystallite sizes for SS- and LS-SEs, determined by the Williamson–Hall method,[52] are provided in Table S4, Supporting Information.

Four electrodes were prepared by manually mixing NCM, SE, and super C65 in a weight ratio of 70:30:3, respectively, and the NCM/Li–In all-solid-state half-cells were tested between 3.0 and 4.3 V (vs Li/Li$^+$) at 30 °C (**Figure 2**). The cells were assembled at a fabricating pressure of 370 MPa and tested at an operating (or stack) pressure of 70 MPa. The results are summarized in Table S5, Supporting Information. Figure 2a,b show the first charge–discharge voltage profiles at 0.2C for the SS-SE and LS-SE samples, respectively. The electrode with SS-LPSnS showed a higher first discharge capacity (138 mA h g^{-1}) than that of the electrode with SS-LPS (120 mA h g^{-1}) (Figure 2a), which can be explained using the higher Li^+ conductivity of SS-LPSnS (0.77 mS cm^{-1}) than that of SS-LPS (0.41 mS cm^{-1}). The slightly higher capacity for using LS-LPS (165 mA h g^{-1}) than that for using LS-LPSnS (159 mA h g^{-1}) can also be rationalized by the higher Li^+ conductivity of LS-LPS (0.24 mS cm^{-1}) than that of LS-LPSnS (0.19 mS cm^{-1}) (Figure 2b). However, when comparing the performance of the SS-SE and LS-SE samples, the difference in ionic conductivities of the SEs fails to explain the significantly higher capacities for using LS-SEs compared to those for using SS-SEs. Initial Coulombic efficiencies (ICEs) for using LS-SEs were also higher than those for using SS-SEs (Table S5 and Figure S8, Supporting Information). Moreover, cycling retention for using LS-SEs (92.6% and 91.7% for LS-LPS and LS-LPSnS, respectively) was significantly superior to that for using SS-SEs (79.6 and 72.8% for SS-LPSnS and SS-LPS, respectively) (Figure 2c). As this intriguing result indicates a distinct effect of the synthetic protocol on the electrochemical performance, a control experiment was performed. After the SS-LPS powder was dispersed in THF overnight, the solvent evaporated, followed by HT at 260 °C under vacuum. Although the SE powder lost its crystallinity immediately after solvent removal, the original phase was recovered after HT (Figure S9, Supporting Information). Notably, when tested in NCM/Li–In all-solid-state half-cells, the electrode employing the THF-treated SS-LPS exhibited a significantly higher capacity (165 mA h g^{-1}, dashed line, Figure 2a) than that for using pristine SS-LPS (120 mA h g^{-1}). Also, the capacity retention after 150 cycles for the THF-treated SS-LPS (92.4%) was similar to that for using LS-LPS (92.6%, Figure S10, Supporting Information).

The distinctly better performance of the electrodes using LS-SEs (or THF-treated SS-LPS) over those using SS-SEs demonstrates the significant effect of the synthesis history of SEs, which prompted us to investigate its origin. First, the particle-size distributions and/or electrochemical stability of the SE samples may be one of the origins, which are discussed later. Second, the residual organic species remaining in the LS-SEs may cause a difference in electrochemical performance. Thus, the organic impurities in the four SE samples were quantified using elemental analysis (Table S2, Supporting Information). Not surprisingly, the weight fractions of organic carbon in LS-SEs were significantly higher (2.97 and 2.06 wt% for LS-LPS and LS-LPSnS, respectively) than those in SS-SEs (0.06 wt%). These "soft" organic residues could significantly affect the mechanical properties of SEs and thus their electrochemical performance by alleviating detrimental electrochemo-mechanical degradation. Therefore, we extensively characterized the mechanical properties of the SS- and LS-SE samples.

ADVANCED
SCIENCE NEWS

www.advancedsciencenews.com

ADVANCED
ENERGY
MATERIALS

www.advenergymat.de

Figure 2. Electrochemical performance of NCM/Li–In all-solid-state half-cells at 0.2C and 30 °C. a) First-cycle charge–discharge voltage profiles for using SS-LPS and SS-LPSnS. Data for using SS-LPS treated using THF is also compared. b) First-cycle charge–discharge voltage profiles for using LS-LPS and LS-LPSnS. c) Cycling performance for using SS-LPS, SS-LPSnS, LS-LPS, and LS-LPSnS.
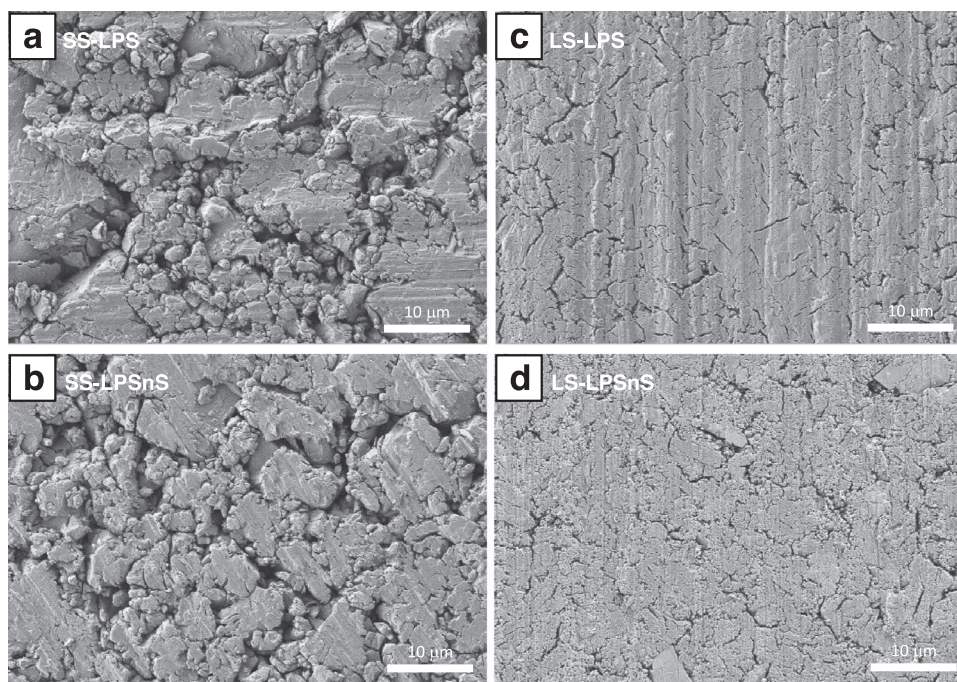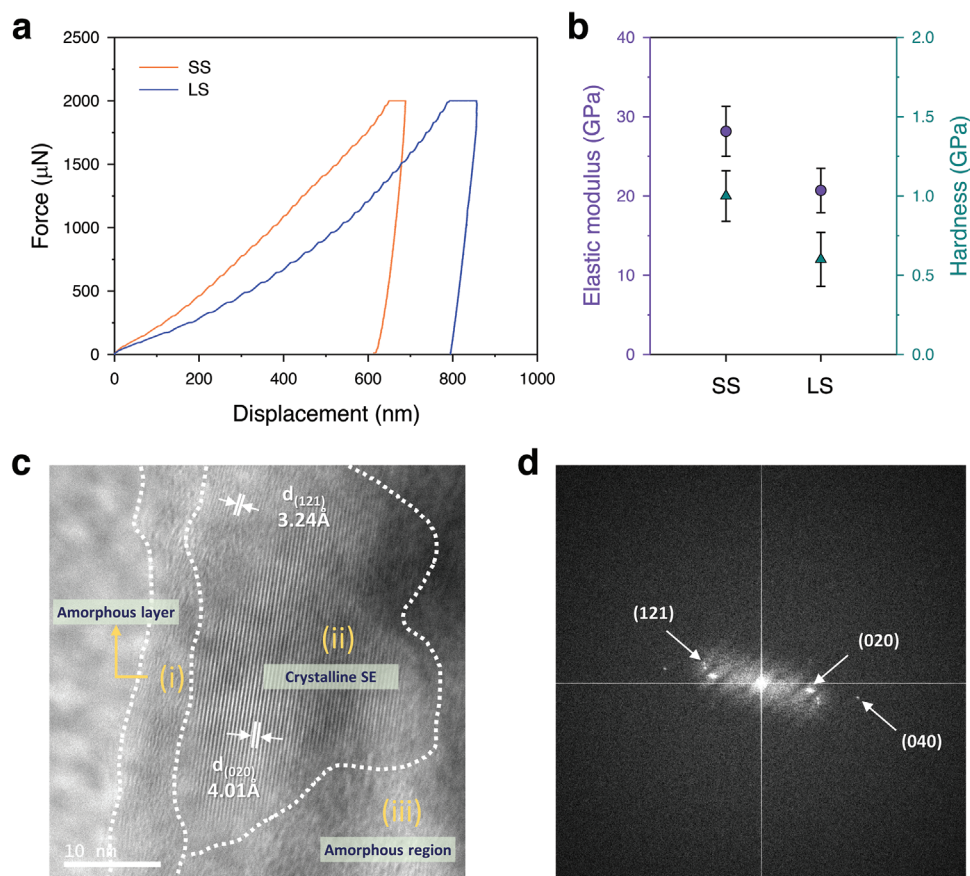
Figure 3. SEM top-view images of cold-pressed pellets for a) SS-LPS, b) SS-LPSnS, c) LS-LPS, and d) LS-LPSnS.

SEM images of the four SE pellets prepared at 370 MPa are shown in **Figure 3** and Figure S11, Supporting Information. The LS-SE pellets (Figure 3c,d) show significantly less void space compared to the SS-SE pellets (Figure 3a,b), indicating a better deformability of LS-SEs than that of SS-SEs. Consistently, the densities of the cold-pressed pellets for LS-SEs were higher than those for SS-SEs: 1.80 g cm^{-3} for LS-LPS versus 1.68 g cm^{-3} for SS-LPS and 1.97 g cm^{-3} LS-LPSnS versus 1.80 g cm^{-3} for SS-LPSnS (Table S2, Supporting Information). Considering that organic residues included in LS-SEs would be lighter than SE phases, the even higher pellet densities of LS-SEs than those of SS-SEs indicate less porosity, reflecting a better deformability of LS-SEs compared to SS-SEs. Furthermore, the mechanical properties of the LPSnS pellets derived via different synthetic routes were quantified using the nano-indentation method (**Figure 4**a,b). Figure 4a shows a representative force–displacement curve at room temperature. At the peak load of 2000 µN, LS-LPSnS exhibited a displacement value of 800 nm, which is larger than that of SS-LPSnS (600 nm), indicating higher deformability. Moreover, the modulus and hardness of LS-LPSnS were 20 and 0.6 GPa, respectively, which are significantly lower than those of SS-LPSnS (28 and 1.0 GPa) (Figure 4b). The microstructure of LS-LPSnS was investigated using cryo-TEM (Figure 4c,d).[53–55] A high-resolution image and corresponding fast Fourier transform (FFT) pattern reveal the presence of multiple phases composed of crystalline and amorphous phases with different morphologies. Scanning TEM-energy dispersive X-ray spectroscopy (EDXS) elemental maps of the LS-LPSnS particle are also shown in Figure S12, Supporting Information. The uniform distribution of P, S, Sn, and C elements is validated. The lattice spacing from the surface to the crystalline parts was also measured (Figure S13a, Supporting Information). The patterns at the surface region exhibit short-range ordering around 3 Å (Figure S13b, Supporting Information).[56,57] It is considered that the amorphous regions (Figure 4c[i,iii]) consist of amorphous SE phase and/or organic species. Importantly, the organic species is believed to promote the deformation of SE particles under the applied pressure.

To assess the electrochemical performance according to the mechanical properties of the SEs, NCM electrodes using SS-LPSnS or LS-LPSnS were assembled under a low fabricating pressure (148 vs 370 MPa) and/or tested under low operating pressure (12 MPa), and the results are summarized in **Figure 5**. Figure 5a,b shows the first-cycle charge–discharge voltage profiles at 0.2C and 30 °C for NCM electrodes tailored under different fabricating pressures. Corresponding cycling performance and Coulombic efficiency (CE) results are shown in Figure S14, Supporting Information. The operating pressure in the corresponding tests was 70 MPa. When the fabricating pressure was reduced from 370 to 148 MPa, the capacity decay for using SS-LPSnS was ≈41 mA h g^{-1} (Figure 5a), which is in stark contrast to the marginal capacity loss incurred when using LS-LPSnS (Figure 5b). Cross-sectional SEM images of the NCM electrodes fabricated using SS-LPSnS and LS-LPSnS at 148 MPa are shown in Figure 5c,d, respectively (high-magnification images and corresponding EDXS elemental maps are shown in Figure S15, Supporting Information). The large void spaces at the interfaces between the NCM and SS-LPSnS particles indicate insufficient ionic contact (Figure 5c). By contrast, the NCM and LS-LPSnS particles exhibit significantly fewer void spaces, reflecting better ionic contact (Figure 5d). Therefore, the capacity varying with the fabricating pressure is attributed to the different deformability of the catholytes: SS-LPSnS < LS-LPSnS.

When a low operating pressure (12 MPa) was applied at the ASLB cells, the NCM electrode with LS-LPSnS exhibited

ADVANCED
SCIENCE NEWS

www.advancedsciencenews.com

ADVANCED
ENERGY
MATERIALS

www.advenergymat.de

Figure 4. Mechanical properties and HRTEM results for LPSnS prepared by solid-state synthesis or liquid-phase synthesis. a) Quasi-static nanoindentation curves and b) elastic modulus and hardness of SS- and LS-LPSnS pellets. c) HRTEM image of LS-LPSnS and d) corresponding FFT pattern.

better performance than that with SS-LPSnS (Figure 5e,f). The initial discharge capacity at 12 MPa for using SS-LPSnS was 137 mA h g^{-1}, which is similar to that under an operating pressure of 70 MPa. However, the capacity retention after 150 cycles at 12 MPa was 70.7%, which is significantly lower than that at 70 MPa (79.6%). By stark contrast, the NCM electrode with LS-LPSnS operated at 12 MPa showed a first-discharge capacity of 154 mA h g^{-1} and a capacity retention of 89.6%, which are similar to those observed at 70 MPa (159 mA h g^{-1} and 91.7%, respectively). Consistently, the ICE for using LS-LPSnS at 12 MPa was also higher than that for using SS-LPSnS (76.2% vs 69.2%, Table S5 and Figure S16, Supporting Information). Further decrease of the operating pressure down to practically acceptable value of 3 MPa resulted in more drastic difference in the electrochemical performance between the electrodes using LS-LPSnS and SS-LPSnS (Figure S17, Supporting Information). The initial discharge capacities at 3 MPa for using SS-LPSnS and LS-LPSnS were similar to those at 12 MPa. However, for using SS-LPSnS, the capacity retention after ten cycles at 3 MPa was 89.4% which is lower than that at 12 MPa (91.0%). By contrast, for using LS-LPSnS, the capacity retention at 3 and 12 MPa remained comparable: 97.0% and 97.3%, respectively. Figure S18, Supporting Information, summarizes the capacity retention after ten cycles for using SS-LPSnS and LS-LPSnS with the three different operating pressures. The more severe degradation for using SS-LPSnS at lower operating pressure

compared to that for using LS-LPSnS is confirmed. In summary, the electrochemical performance under low fabricating or operating pressures demonstrate dramatically better performance using LS-SEs compared to SS-SEs. This performance is attributed to the better deformability of LS-SEs, which are effective in reducing detrimental electrochemo-mechanical degradation.[58]

Despite the successful demonstration of the distinct effect of the improved deformability of LS-SEs over SS-SEs on the electrochemical performance of all-solid-state cells, other factors were also investigated. First, the electrochemical stability of LS-LPSnS, tested by cyclic voltammetry (CV), was slightly inferior to that of SS-LPSnS (Figure S19, Supporting Information). Second, to assess the particle size effect, a control experiment was performed. SEM images of the four SE powders shown in Figure S20, Supporting Information, exhibit a few to tens of micrometer particle sizes. The LS-LPSnS powders were sieved using a mesh with an opening size of 25 μm. Then, the powders that remained unsieved were collected (referred to as "L-LS-LPSnS"). They exhibit large particle sizes of hundreds of micrometers (Figure S21a, Supporting Information). Using these large particles (L-LS-LPSnS) as the catholyte, NCM/Li–In all-solid-state half-cells were fabricated under 370 or 148 MPa and tested at 70 MPa at 30 °C (Figure S21b, Supporting Information). The first-cycle discharge capacities for using L-LS-LPSnS with the fabricating pressures of 370 and

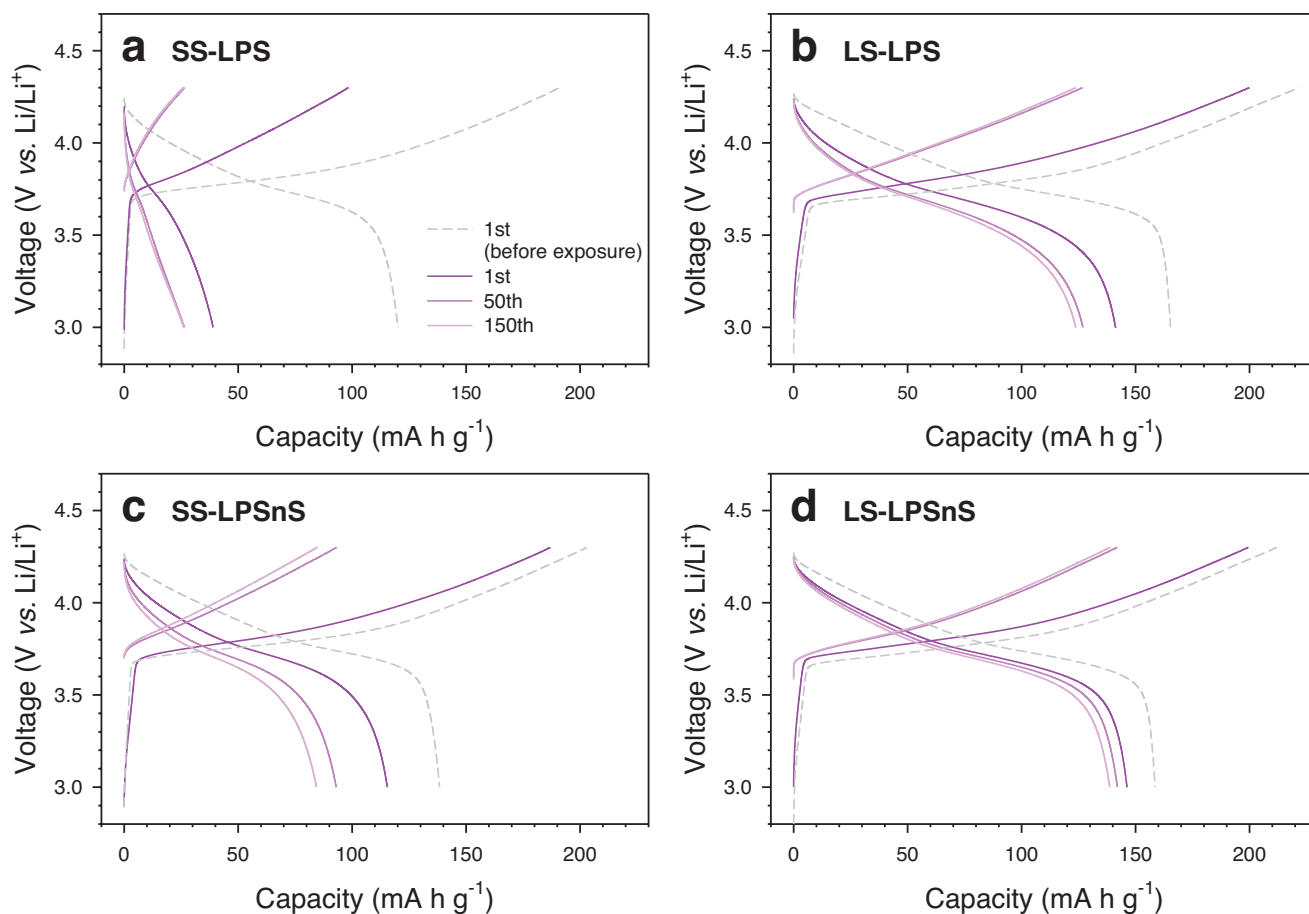**Varying fabricating P (operating P = 70 MPa)**
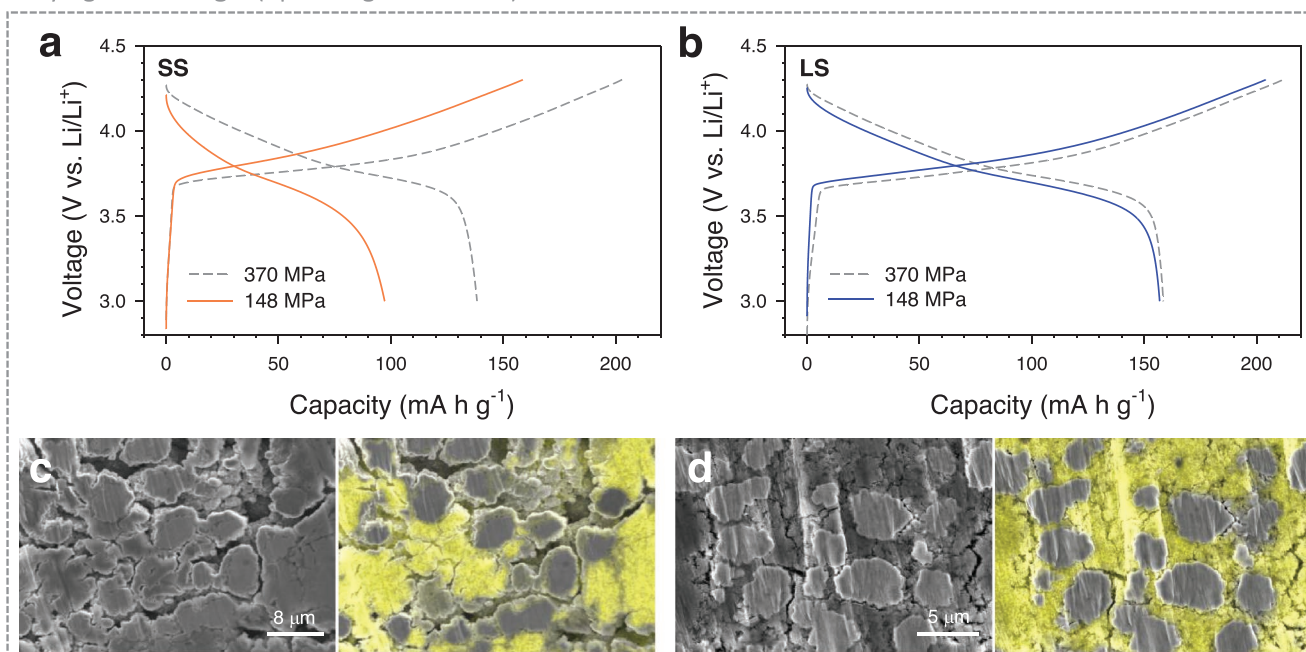
Operating P = 12 MPa
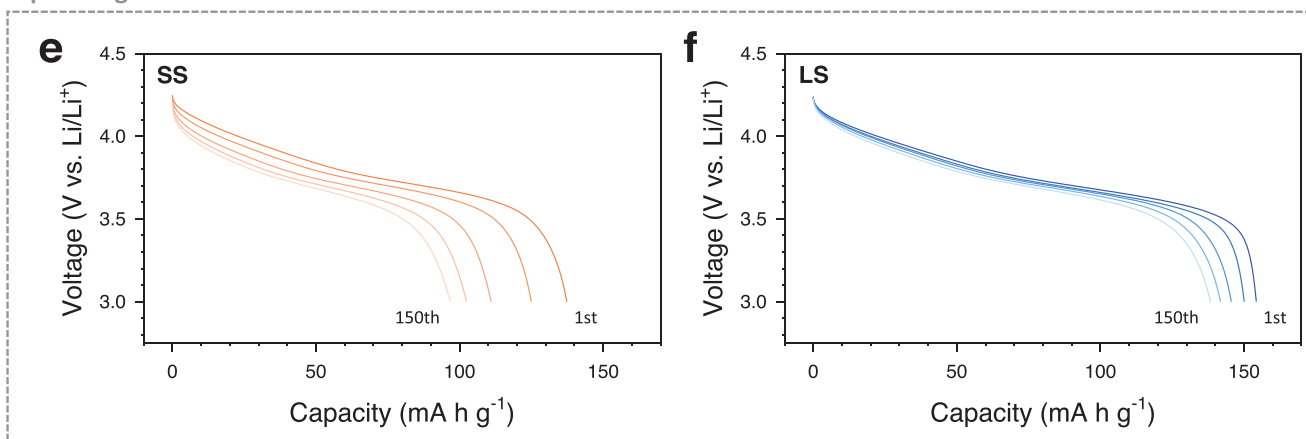
Figure 5. Electrochemical performance of NCM/Li–In all-solid-state half-cells at 0.2C and 30 °C with variation in the fabricating and operating pressures, for using LPSnS catholytes prepared by solid-state synthesis or liquid-phase synthesis. First-cycle charge–discharge voltage profiles for the fabricating pressures of 370 and 148 MPa, at an operating pressure of 70 MPa for using catholytes prepared by a) solid-state synthesis and b) liquid-phase synthesis. The cross-sectional SEM images of NCM electrodes using catholytes prepared by c) solid-state synthesis and d) liquid-phase synthesis, at 148 MPa. In (c) and (d), yellow-colored SE regions correspond to the SEM EDXS signal of sulfur. Discharge voltage profiles at 1st, 10th, 50th, 100th, and 150th cycles at an operating pressure of 12 MPa, for using catholytes prepared by e) solid-state synthesis and f) liquid-phase synthesis. The fabricating pressure for the cells was 370 MPa.

148 MPa were 161 and 146 mA h g^{-1}, respectively. These values are comparable or slightly lower than the capacities for the electrodes using LS-LPSnS: 159 and 157 mA h g^{-1}, respectively (Figure 5b). However, they are significantly larger than those for the electrodes using SS-LPSnS: 138 and 97 mA h g^{-1}, respectively (Figure 5a). Considering that the particle sizes of L-LS-LPSnS were much larger than SS-LPSnS, the much higher capacity for using L-LS-LPSnS than that for using SS-LPSnS is explained by the better deformability of L-LS-LPSnS than that of SS-LPSnS. In conclusion, although the particle size distribution also affects the electrochemical performance

under the low fabricating pressure, their contribution is not as much as the mechanical deformability.

Finally, the air stability of the four SEs and their effect on the electrochemical performance were evaluated. The SE powders were exposed to dry air (dew point of −20 °C) for 5 h. The XRD patterns of the SEs before and after air exposure are shown in Figure S22, Supporting Information. Notably, SS-LPS and LS-LPS produce unknown impurities and/or Li$_2$S, which are absent in SS-LPSnS and LS-LPSnS. The electrochemical performance of NCM/Li–In half-cells at 0.2C and 30 °C for NCM electrodes employing air-exposed SEs is shown in **Figure 6** and

**ADVANCED
SCIENCE NEWS**

www.advancedsciencenews.com

**ADVANCED
ENERGY
MATERIALS**

www.advenergymat.de

Figure 6. Air-stability results of LPS and LPSnS. Charge–discharge voltage profiles of NCM/Li–In all-solid-state half-cells at 0.2C and 30 °C for using a) SS-LPS, b) LS-LPS, c) SS-LPSnS, and d) LS-LPSnS. Data for using pristine catholytes (dashed lines) are also compared.

Figure S23, Supporting Information. The first-discharge capacity retention after air exposure is in the following order SS-LPS (32.5%) << SS-LPSnS (83.4%) < LS-LPS (85.4%) < LS-LPSnS (92.2%). This result confirms the beneficial effect of Sn substitution on air stability. The superior performance of LS-SEs over SS-SEs is also noteworthy. It is considered that the organic species remaining in the LS-SEs might impede air permeation through the bulk SEs.[59]

3. Conclusion

In summary, glass-ceramic LPSnS (0.19 mS cm^{-1} at 30 °C) was successfully prepared via a liquid-phase route using EDA–EDT with THF, which acted as the reaction medium, providing a strong dissolving power and stirring mediation, respectively, and synergistically promoted the liquid-phase reaction. SEM, elemental, nano-indentation, and cryo-TEM analyses revealed the superior deformability of LS-SEs over SS-SEs, originating from the remaining marginal organic species. When employed as the catholyte for NCM electrodes in all-solid-state cells, the LS-SEs exhibited remarkably better performance than SS-SEs, particularly when assembled under a low fabricating pressure (148 vs 370 MPa) or tested under low operating pressures (12 or

3 MPa). These results are attributed to the better deformability of LS-SEs over SS-SEs, which can reduce detrimental electro-chemo-mechanical degradation. Finally, it was demonstrated that SEs prepared by LS (vs SS) or using Sn-substituted composition (LPSnS vs LPS) show better air stability. It is emphasized that we explored the unprecedented advantages of the LS of sulfide SEs. The relatively low Li$^+$ conductivity of LS-LPSnS can be compensated by using them with highly conductive SEs for practical applications: the ductile LS-LPSnS and highly conductive SE can synergistically promote ionic contact and fast Li$^+$ transport, respectively. We believe that our findings provide important guidelines for the development of advanced SE materials for practical all-solid-state batteries.

4. Experimental Section

Material Preparation: To synthesize SS-LPS and SS-LPSnS powders, a stoichiometric mixture of Li$_2$S (99.9%, Alfa Aesar), P$_2$S$_5$ (99%, Sigma Aldrich), and SnS$_2$ (99%, MKN, for the preparation of SS-LPSnS only) was ball-milled at 500 rpm in a zirconia vial with ZrO$_2$ balls (5 mm in diameter) using Pulverisette 7 PL (Fritsch GmbH), followed by HT in a glass ampoule sealed under vacuum at 240 °C for 1 h. LS-LPS was obtained via a liquid-phase route using THF (99.9%, anhydrous, Sigma-Aldrich). A stoichiometric mixture of Li$_2$S and P$_2$S$_5$ suspended in

THF (81.6 mg mL^{-1}) was stirred at 30 °C overnight, followed by drying at 80 °C for 6 h and subsequent HT at 140 °C for 1 h under vacuum. LS-LPSnS was obtained via a liquid-phase route using THF, EDA (98.5%, Sigma-Aldrich), and EDT (98.0%, Sigma-Aldrich). A stoichiometric SnS$_2$ solution (in EDA–EDT, 10:1 vol. ratio, 50.1 mg mL^{-1}) was added to a stoichiometric Li$_2$S-P$_2$S$_5$ suspension in THF and stirred at 70 °C overnight, followed by drying at 180 °C for 6 h and subsequent HT at 260 °C for 5 h under vacuum. For preparation of Li$_6$PS$_5$Cl$_{0.5}$Br$_{0.5}$, after a stoichiometric mixture of Li$_2$S, P$_2$S$_5$, LiCl (99.99%, Alfa-Aesar), and LiBr (99.99%, Alfa-Aesar) was ball-milled at 600 rpm for 10 h in a ZrO$_2$ vial with ZrO$_2$ balls (10 mm in diameter) using Pulverisette 7 PL (Fritsch GmbH), followed by HT 550 °C for 5 h under an Ar atmosphere.

Material Characterization: Structural characterization of the SE powders was performed by powder XRD measurements using a Rigaku MiniFlex600 with Cu-K$_\alpha$ radiation (λ = 1.5406 Å) at 40 kV and 15 mA. XRD measurements were conducted using an airtight container with a beryllium window without exposure to air. To evaluate the constituents in the SEs, XRD data were refined by the Rietveld refinement method using the Fullprof software. The structural parameters of ZnO crystal, as a reference material, and the SEs were obtained from Rietveld analysis. The XRD patterns of mixtures of SE and ZnO in a weight ratio of 50:50 were used for quantification of the crystalline and amorphous phases. Weight ratios of ZnO crystal to each crystal were calculated using the Rietveld refinement method. For FESEM-BSE measurements, the NCM composites were collected in an Ar-filled glovebox and polished using an Ar-ion beam at 6 kV for 8 h and subsequently at 4 kV for 2 h at −100 °C (JEOL, IB-19510CP). The polished samples were transferred to FESEM equipment without air exposure. For the nanoindentation tests, SE pellets (diameter = 6 mm) were prepared via uniaxial pressing at 370 MPa. Equations for obtaining modulus are described in Supporting Information. The controlled indentation load was a maximum force of 2000 µN using a PI-85 instrument (Bruker Corp.). For cryo-TEM measurements, LS-LPSnS powder samples were loaded onto a lacey Cu grid. To avoid exposure to air, a Double-tilt LN2 Atmos Defend Holder (Mel-Build) was employed for cryo-TEM that contained a vacuum transfer function. The cryo-TEM images were obtained using a JEM-2100F (JEOL) instrument at an acceleration voltage of 200 kV. For the air-exposure test, 250 mg of SE samples were exposed to air with a dew point of −20 °C for 5 h using a custom-made test box. The electronic conductivity of the SE pellets prepared at 370 MPa was measured using the van der Pauw method.[60]

Electrochemical Characterization: A LiNbO$_3$-coated NCM powder was used in this study. Composite electrodes were prepared by mixing NCM, SEs, and Super C65 at a weight ratio of 7:3:0.3. Li$_{0.5}$In (nominal composition) powder as the counter/reference electrode was prepared by ball-milling Li powder (FMC Lithium Corp.) and In powder (Sigma-Aldrich, 99%). The NCM electrode (15 mg) and Li–In electrode (80 mg) were placed on each side of the pre-pelletized Li$_6$PS$_5$Cl$_{0.5}$Br$_{0.5}$ layer (150 mg) and pressed at a fabrication pressure of 148 or 370 MPa at room temperature. Finally, the external pressure of the all-solid-state cells during operation was 3 or 12 or 70 MPa. For the operating pressure of 3 MPa, to facilitate electrical contacts between Ti rods and electrodes, a super C65 layer was placed in between Ti rods and electrodes. All assemblies were carried out in a poly(aryl-ether-ether-ketone) mold with a 13 mm diameter and two Ti rods as the current collectors. All NCM/Li–In cells were cycled between 3.0 and 4.3 V (vs Li/Li$^+$) at 30 °C. For CV measurements, a pelletized mixture of SE and Super C65 at a weight ratio of 10:1 was used as the working electrode while the Li$_6$PS$_5$Cl$_{0.5}$Br$_{0.5}$ layer and Li–In electrode were employed as the separating SE layer and counter/reference electrode, respectively.

Supporting Information

Supporting Information is available from the Wiley Online Library or from the author.

Conflict of Interest

The authors declare no conflict of interest.

Data Availability Statement

The data that support the findings of this study are available on request from the corresponding author.

[1] J. Janek, W. Zeier, *Nat. Energy* **2016**, *1*, 16141.
[2] A. Manthiram, X. Yu, S. Wang, *Nat. Rev. Mater.* **2017**, *2*, 16103.
[3] K. H. Park, Q. Bai, D. H. Kim, D. Y. Oh, Y. Zhu, Y. Mo, Y. S. Jung, *Adv. Energy Mater.* **2018**, *8*, 1800035.
[4] S. Chen, D. Xie, G. Liu, J. P. Mwizerwa, Q. Zhang, Y. Zhao, X. Xu, X. Yao, *Energy Storage Mater.* **2018**, *14*, 58.
[5] M. J. Wang, R. Choudhury, J. Sakamoto, *Joule* **2019**, *3*, 2165.
[6] R. Pfenninger, M. Struzik, I. Garbayo, E. Stilp, J. L. M. Rupp, *Nat. Energy* **2019**, *4*, 475.
[7] Q. Zhang, D. Cao, Y. Ma, A. Natan, P. Aurora, H. Zhu, *Adv. Mater.* **2019**, *31*, 1901131.
[8] L. Duchêne, A. Remhof, H. Hagemann, C. Battaglia, *Energy Storage Mater.* **2020**, *25*, 782.
[9] R. Chen, Q. Li, X. Yu, L. Chen, H. Li, *Chem. Rev.* **2020**, *120*, 6820.
[10] L.-Z. Fan, H. He, C.-W. Nan, *Nat. Rev. Mater.* **2021**, *6*, 1003.
[11] J. A. Lewis, F. J. Q. Cortes, Y. Liu, J. C. Miers, A. Verma, B. S. Vishnugopi, J. Tippens, D. Prakash, T. S. Marchese, S. Y. Han, C. Lee, P. P. Shetty, H.-W. Lee, P. Shevchenko, F. De Carlo, C. Saldana, P. P. Mukherjee, M. T. McDowell, *Nat. Mater.* **2021**, *20*, 503.
[12] Y. Kato, S. Hori, T. Saito, K. Suzuki, M. Hirayama, A. Mitsui, M. Yonemura, H. Iba, R. Kanno, *Nat. Energy* **2016**, *1*, 16030.
[13] D. H. S. Tan, Y. S. Meng, J. Jang, *Joule* **2022**, *6*, 1755.
[14] H. Muramatsu, A. Hayashi, T. Ohtomo, S. Hama, M. Tatsumisago, *Solid State Ionics* **2011**, *182*, 116.
[15] H. Kwak, K. H. Park, D. Han, K.-W. Nam, H. Kim, Y. S. Jung, *J. Power Sources* **2020**, *446*, 227338.
[16] G. Sahu, Z. Lin, J. Li, Z. Liu, N. Dudney, C. Liang, *Energy Environ. Sci.* **2014**, *7*, 1053.
[17] Z. Yu, S.-L. Shang, J.-H. Seo, D. Wang, X. Luo, Q. Huang, S. Chen, J. Lu, X. Li, Z.-K. Liu, D. Wang, *Adv. Mater.* **2017**, *29*, 1605561.

**ADVANCED
SCIENCE NEWS**

www.advancedsciencenews.com

**ADVANCED
ENERGY
MATERIALS**

www.advenergymat.de

[18] F. Zhao, S. H. Alahakoon, K. Adair, S. Zhang, W. Xia, W. Li, C. Yu, R. Feng, Y. Hu, J. Liang, X. Lin, Y. Zhao, X. Yang, T.-K. Sham, H. Huang, L. Zhang, S. Zhao, S. Lu, Y. Huang, X. Sun, *Adv. Mater.* **2021**, *33*, 2006577.

[19] L. Ye, E. Gil-González, X. Li, *Electrochem. Commun.* **2021**, *128*, 107058.

[20] K. H. Park, D. Y. Oh, Y. E. Choi, Y. J. Nam, L. Han, J.-Y. Kim, H. Xin, F. Lin, S. M. Oh, Y. S. Jung, *Adv. Mater.* **2016**, *28*, 1874.

[21] Z. Liu, W. Fu, E. A. Payzant, X. Yu, Z. Wu, N. J. Dudney, J. Kiggans, K. Hong, A. J. Rondinone, C. Liang, *J. Am. Chem. Soc.* **2013**, *135*, 975.

[22] A. Miura, N. C. Rosero-Navarro, A. Sakuda, K. Tadanaga, N. H. H. Phuc, A. Matsuda, N. Machida, A. Hayashi, M. Tatsumisago, *Nat. Rev. Chem.* **2019**, *3*, 189.

[23] J. Xu, L. Liu, N. Yao, F. Wu, H. Li, L. Chen, *Mater. Today Nano* **2019**, *8*, 100048.

[24] M. Ghidiu, J. Ruhl, S. P. Culver, W. G. Zeier, *J. Mater. Chem. A* **2019**, *7*, 17735.

[25] F. Marchini, B. Porcheron, G. Rousse, L. A. Blanquer, L. Droguet, D. Foix, T. Koç, M. Deschamps, J. M. Tarascon, *Adv. Energy Mater.* **2021**, *11*, 2101111.

[26] H. Wang, L. Wu, B. Xue, F. Wang, Z. Luo, X. Zhang, L. Calvez, P. Fan, B. Fan, *ACS Appl. Mater. Interfaces* **2022**, *14*, 15214.

[27] S. Ohsaki, T. Yano, A. Hatada, H. Nakamura, S. Watano, *Powder Technol.* **2021**, *387*, 415.

[28] H.-D. Lim, X. Yue, X. Xing, V. Petrova, M. Gonzalez, H. Liu, P. Liu, *J. Mater. Chem. A* **2018**, *6*, 7370.

[29] R. C. Xu, X. H. Xia, Z. J. Yao, X. L. Wang, C. D. Gu, J. P. Tu, *Electrochim. Acta* **2016**, *219*, 235.

[30] M. Calpa, N. C. Rosero-Navarro, A. Miura, K. Tadanaga, *RSC Adv.* **2017**, *7*, 46499.

[31] N. H. H. Phuc, K. Morikawa, T. Mitsuhiro, H. Muto, A. Matsuda, *Ionics* **2017**, *23*, 2061.

[32] N. H. H. Phuc, M. Totani, K. Morikawa, H. Muto, A. Matsuda, *Solid State Ionics* **2016**, *288*, 240.

[33] S. Ito, M. Nakakita, Y. Aihara, T. Uehara, N. Machida, *J. Power Sources* **2014**, *271*, 342.

[34] Y. Wang, Z. Liu, X. Zhu, Y. Tang, F. Huang, *J. Power Sources* **2013**, *224*, 225.

[35] S. Chida, A. Miura, N. C. Rosero-Navarro, M. Higuchi, N. H. H. Phuc, H. Muto, A. Matsuda, K. Tadanaga, *Ceram. Int.* **2018**, *44*, 742.

[36] H. Wang, Z. D. Hood, Y. Xia, C. Liang, *J. Mater. Chem. A* **2016**, *4*, 8091.

[37] Z. Wang, Y. Jiang, J. Wu, Y. Jiang, S. Huang, B. Zhao, Z. Chen, J. Zhang, *Chem. Eng. J.* **2020**, *393*, 124706.

[38] Y. Wang, D. Lu, M. Bowden, P. Z. El Khoury, K. S. Han, Z. D. Deng, J. Xiao, J.-G. Zhang, J. Liu, *Chem. Mater.* **2018**, *30*, 990.

[39] M. Calpa, N. C. Rosero-Navarro, A. Miura, K. Terai, F. Utsuno, K. Tadanaga, *Chem. Mater.* **2020**, *32*, 9627.

[40] L. Zhou, K.-H. Park, X. Sun, F. Lalère, T. Adermann, P. Hartmann, L. F. Nazar, *ACS Energy Lett.* **2019**, *4*, 265.

[41] J. E. Lee, K.-H. Park, J. C. Kim, T.-U. Wi, A. R. Ha, Y. B. Song, D. Y. Oh, J. Woo, S. H. Kweon, S. J. Yeom, W. Cho, K. Kim, H.-W. Lee, S. K. Kwak, Y. S. Jung, *Adv. Mater.* **2022**, *34*, 2200083.

[42] J. Lee, T. Lee, K. Char, K. J. Kim, J. W. Choi, *Acc. Chem. Res.* **2021**, *54*, 3390.

[43] Y. B. Song, H. Kwak, W. Cho, K. S. Kim, Y. S. Jung, K.-H. Park, *Curr. Opin. Solid State Mater. Sci.* **2022**, *26*, 100977.

[44] X. Gao, B. Liu, B. Hu, Z. Ning, D. S. Jolly, S. Zhang, J. Perera, J. Bu, J. Liu, C. Doerrer, E. Darnbrough, D. Armstrong, P. S. Grant, P. G. Bruce, *Joule* **2022**, *6*, 636.

[45] T. Y. Kwon, K. T. Kim, D. Y. Oh, Y. B. Song, S. Jun, Y. S. Jung, *Energy Storage Mater.* **2022**, *49*, 219.

[46] R. Koerver, W. Zhang, L. de Biasi, S. Schweidler, A. O. Kondrakov, S. Kolling, T. Brezesinski, P. Hartmann, W. G. Zeier, J. Janek, *Energy Environ. Sci.* **2018**, *11*, 2142.

[47] A. Kato, M. Yamamoto, A. Sakuda, A. Hayashi, M. Tatsumisago, *ACS Appl. Energy Mater.* **2018**, *1*, 1002.

[48] K. Homma, M. Yonemura, T. Kobayashi, M. Nagao, M. Hirayama, R. Kanno, *Solid State Ionics* **2011**, *182*, 53.

[49] F. Mizuno, A. Hayashi, K. Tadanaga, M. Tatsumisago, *Adv. Mater.* **2005**, *17*, 918.

[50] C. Dietrich, D. A. Weber, S. J. Sedlmaier, S. Indris, S. P. Culver, D. Walter, J. Janek, W. G. Zeier, *J. Mater. Chem. A* **2017**, *5*, 18111.

[51] S. Yubuchi, H. Tsukasaki, A. Sakuda, S. Mori, A. Hayashi, M. Tatsumisago, *RSC Adv.* **2019**, *9*, 14465.

[52] A. K. Zak, W. H. A. Majid, M. E. Abrishami, R. Yousefi, *Solid State Sci.* **2011**, *13*, 251.

[53] Y. Li, Y. Li, A. Pei, K. Yan, Y. Sun, C.-L. Wu, L.-M. Joubert, R. Chin, L. K. Ai, Y. Yu, J. Perrino, B. Butz, S. Chu, Y. Cui, *Science* **2017**, *358*, 506.

[54] C. Fang, J. Li, M. Zhang, Y. Zhang, F. Yang, J. Z. Lee, M.-H. Lee, J. Alvarado, M. A. Schroeder, Y. Yang, B. Lu, N. Williams, M. Ceja, L. Yang, M. Cai, J. Gu, K. Xu, X. Wang, Y. S. Meng, *Nature* **2019**, *572*, 511.

[55] Y. B. Song, D. H. Kim, H. Kwak, D. Han, S. Kang, J. H. Lee, S.-M. Bak, K.-W. Nam, H.-W. Lee, Y. S. Jung, *Nano Lett.* **2020**, *20*, 4337.

[56] F. Wu, J. T. Lee, E. Zhao, B. Zhang, G. Yushin, *ACS Nano* **2016**, *10*, 1333.

[57] M. Ghazinejad, S. Holmberg, O. Pilloni, L. Oropeza-Ramos, M. Madou, *Sci. Rep.* **2017**, *7*, 16551.

[58] M. Papakyriakou, M. Lu, Y. Liu, Z. Liu, H. Chen, M. T. McDowell, S. Xia, *J. Power Sources* **2021**, *516*, 230672.

[59] X. Lu, O. Camara, Z. Liu, A. Windmüller, C.-L. Tsai, H. Tempel, S. Yu, H. Kungl, R.-A. Eichel, *Electrochem. Sci. Adv.* **2022**, e2100208.

[60] L. J. van der Pauw, *Philips Tech. Rev.* **1958**, *20*, 220.